Publication Year	2023
Acceptance in OA	2025-02-06T15:30:20Z
Title	Optical and Infrared Counterparts of the X-Ray Sources Detected in the Chandra Cygnus OB2 Legacy Survey
Authors	GUARCELLO, Mario Giuseppe, Drake, J. J., Wright, N. J., Naylor, T., FLACCOMIO, Ettore, Kashyap, V. L., García-Alvarez, D.
Publisher's version (DOI)	10.3847/1538-4365/acdd64
Handle	http://hdl.handle.net/20.500.12386/35830
Journal	THE ASTROPHYSICAL JOURNAL SUPPLEMENT SERIES
Volume	269

The Astrophysical Journal Supplement Series, 269:9 (15pp), 2023 November https://doi.org/10.3847/1538-4365/acdd64

Optical and Infrared Counterparts of the X-Ray Sources Detected in the Chandra Cygnus OB2 Legacy Survey

M. G. Guarcello[1,2], J. J. Drake[2], N. J. Wright[2,3], T. Naylor[4], E. Flaccomio[1], V. L. Kashyap[2], and D. García-Alvarez[5,6,7]
[1] INAF—Osservatorio Astronomico di Palermo, Piazza del Parlamento 1, I-90134, Palermo, Italy; mario.guarcello@inaf.it
[2] Smithsonian Astrophysical Observatory, MS-67, 60 Garden Street, Cambridge, MA 02138, USA
[3] Astrophysics Group, Keele University, Keele ST5 5BG, UK
[4] School of Physics, University of Exeter, Stocker Road, Exeter EX4 4QL, UK
[5] Dpto. de Astrofísica, Universidad de La Laguna, E-38206 - La Laguna, Tenerife, Spain
[6] Grantecan CALP, E-38712 Breña Baja, La Palma, Spain
[7] Instituto de Astrofísica de Canarias, E-38205 La Laguna, Tenerife, Spain

Received 2014 October 31; revised 2014 December 12; accepted 2017 February 2; published 2023 October 25

Abstract

The young massive OB association Cygnus OB2, in the Cygnus X complex, is the closest (∼1400 pc) star-forming region to the Sun hosting thousands of young low-mass stars and up to 1000 OB stars, among which are some of the most massive stars known in our Galaxy. This region holds great importance for several fields of modern astrophysics, such as the study of the physical properties of massive and young low-mass stars and the feedback provided by massive stars on star and planet formation processes. Cyg OB2 has been recently observed with Chandra/ACIS-I as part of the 1.08 Ms Chandra Cygnus OB2 Legacy Project. This survey detected 7924 X-ray sources in a square degree area centered on Cyg OB2. Since a proper classification and study of the observed X-ray sources also requires the analysis of their optical and infrared counterparts, we combined a large and deep set of optical and infrared catalogs available for this region with our new X-ray catalog. In this paper we describe the matching procedure and present the combined catalog containing 5703 sources. We also briefly discuss the nature of the X-ray sources with optical and infrared counterparts using their position in the color–magnitude and color–color diagrams.

Unified Astronomy Thesaurus concepts: Astronomy databases (83); Catalogs (205)

1. Introduction

The study of young stellar clusters, together with the correct classification of their stellar content, generally relies on a combination of available multiwavelength data, from X-rays to optical and infrared. A key aspect of such studies of crowded stellar fields is the procedure adopted for merging the different data sets. It is important to minimize the number of spurious coincidences and false negatives (i.e., sources in one wave band that fail to be matched with their real counterparts in another). A lack of accuracy and completeness in the data merging process might adversely affect source classification and the subsequent interpretation of the results.

When sparse catalogs are matched, the chances of spurious coincidences are reasonably low. In these cases, simple matches based on source positions can be safely adopted. When the source density of one or more of the catalogs is high, such that the probability of finding more than one object within the bounds of a source position uncertainty is deemed significant, the use of more complicated methods that take into account the expected multiwaveband properties of the source populations must be used. To this aim, several maximum likelihood (ML) methods have been proposed in the literature (e.g., Sutherland & Saunders 1992).

Cygnus OB2 is the central massive OB association of the giant Cygnus X complex, with a rich population of young stars spread over an area of more than 1 deg^2. Because of its very rich population of massive stars, Cyg OB2 has been described as a very young globular cluster in the Milky Way (Knödlseder 2000). The census of the massive population of this association ranges from the first count by Reddish et al. (1967) of 300 OB members to the estimate based on Two Micron All Sky Survey (2MASS) data of more than 2600 OB stars by Knödlseder (2000). More recent studies found a somewhat smaller population of massive stars and identified in Cyg OB2 some of the most massive stars known in our Galaxy, such as O3 stars and B supergiants (Walborn 1973; Massey & Thompson 1991; Comerón et al. 2002; Hanson 2003; Negueruela et al. 2008).

Despite the extinction toward Cyg OB2 being high owing to the intervening nebulosity associated with the Cygnus Rift (roughly ranging from $A_V \sim 2.5$ to $A_V \sim 8$ for the optically identified members; Drew et al. 2008; Sale et al. 2009; Guarcello et al. 2012; Sale et al. 2014), its relative proximity (∼1400 pc; Rygl et al. 2012) has made it the subject of several studies aimed at understanding its rich stellar content. Indeed, being the massive association with the largest massive star content in the proximity (i.e., within 2 kpc) of our Sun, with a massive population that has no equal in the other nearby young clusters, such as the Orion Nebula Cluster, and being also rich in pre-main-sequence stars (Albacete Colombo et al. 2007; Wright & Drake 2009; Guarcello et al. 2013), Cyg OB2 is also arguably the best available target to study star formation, disk evolution, and planet formation in the presence of massive stars (e.g., Wright et al. 2014b). The average age of the stars in the central part of the association has been estimated to range between 3 and 5 Myr (Wright et al. 2010), but several new star-forming sites hosting a large fraction of very young stars still embedded in a contracting envelope or thick circumstellar disk have been discovered (Vink et al. 2008; Wright et al. 2012; Guarcello et al. 2013). There are also indications that some OB stars in the association are younger than 2 Myr (Hanson 2003), while a population of A stars found in the southern area appear to have ages between 5 and 7 Myr (Drew et al. 2008).

The promise of Cyg OB2 to be able to shed new light on the workings and products of massive star-forming regions motivated a large Chandra X-ray Observatory 1.08 Ms Legacy Project (Wright et al. 2023a). At ages of a few million years, stars of all masses are about 3 and 4 orders of magnitude stronger X-ray emitters compared with older populations. Hard X-ray photons can penetrate many magnitudes of visual extinction and provide an effective diagnostic of youth that is free from biases resulting from accretion from a protoplanetary disk and the presence of circumstellar material.

The direct aim of the survey was to use the selective power of X-rays together with the arcsecond spatial resolution of Chandra to perform a deep census of the stellar population and its X-ray properties, but with the main scientific goals of understanding the evolution of protoplanetary disks and star formation in an association approaching stellar supercluster dimensions. The resulting Chandra catalog contains 7924 X-ray sources over an area of about 1 deg^2 centered on Cyg OB2 (Wright et al. 2023a). Supplementary optical and infrared data, required to classify the X-ray sources and follow through with the scientific objectives of our survey, have been retrieved from available public surveys (SDSS/DR8, IPHAS/DR2, UKIDSS, 2MASS) and obtained from dedicated observations with OSIRIS@GTC (Guarcello et al. 2012) and Spitzer (Beerer et al. 2010; Guarcello et al. 2013).

A crucial step in being able to use the available multiwavelength catalogs consists of determining which objects in one catalog correspond to sources in another. Given the large stellar density in Cyg OB2, the depth of the OIR catalogs used, and the large foreground and background observed populations, simple nearest neighbor approaches can fail because several potential counterparts can fall within the positional uncertainty of a given source. More sophisticated approaches have employed likelihood ratio methods that seek to utilize other information than simply source position, such as comparative brightness (see, e.g., Richter 1975; Sutherland & Saunders 1992; Smith et al. 2011).

Here we describe the matching of multiwavelength sources to those detected in the Chandra Cyg OB2 survey. A brief overview of the X-ray, optical, and infrared catalogs is presented in Sections 2 and 3; the methods employed to crossmatch objects in different catalogs are described in Section 4; and the final catalog is described in Section 5. We summarize the main points of the study in Section 6.

2. The X-Ray Catalog

The Chandra Cyg OB2 Legacy survey design employed 36 pointings of 30 ks exposure each in a 6 × 6 raster array heavily (∼50%) overlapped in order to overcome the Chandra lower off-axis sensitivity and produce a relatively uniform exposure over the inner 0.5 deg^2 corresponding to a depth of 116 ks. The full survey exposure was 1.08 Ms, covering about 1 deg^2 centered at $20^h 33^m 12^s$, +41 19′00″, and was performed over a 6-week period from 2010 January to March, employing the Advanced CCD Imaging Spectrometer (ACIS-I; Garmire et al. 2003).

The point-source catalog was constructed using a combination of standard CIAO processing tools, source detection algorithms, and the ACIS Extract (AE; Broos et al. 2010) software package. In order to have a homogeneous astrometry among the various Chandra pointings, Chandra astrometry was remapped to that of 2MASS (Cutri et al. 2003) using bright X-ray sources with unambiguous crossmatches to 2MASS objects. Source detection was applied to the reduced and processed Chandra data in three energy bands, soft (0.5–2.0 keV), hard (2.0–7.0 keV), and broad (0.5–7.0 keV), using different algorithms: an enhanced version of the CIAO tool WAVDETECT that performs source detection on multiple nonaligned X-ray observations, detecting sources that may not be detected in the individual observations, and PWDETECT (Damiani et al. 1997). This process was augmented by several hundred sources from lists of known Cyg OB2 members, including O- and B-type stars (Wright et al. 2015b) and young A-type stars (Drew et al. 2008), creating a total of 13,041 source candidates.

Candidate source photometric extraction and validation were performed using AE in an iterative fashion, whereby validated sources were excluded from regions used for background estimation, followed by a repeat of the AE extraction and validation. Due to the overlapping source and background regions in the most crowded areas of the survey, several iterations of this process were required. The resulting X-ray catalog contains 7924 verified sources, the vast majority of which were observed at least 4 times in overlapping tiles and detected within 4′ of the telescope optical axis at least once. The source positional uncertainty is typically <0.″5, and we estimate a 90% completeness for stellar X-ray sources down to an X-ray luminosity of 7×10^{29} erg cm^2 s^{-1} in the central 0.5 deg^2. A full description of the catalog construction is presented by Wright et al. (2023a), while an assessment of the catalog contents and sensitivity is discussed by Wright et al. (2023b).

3. The Optical–Infrared Catalog

The optical–infrared (OIR) catalog used in this work contains photometric data retrieved from several publicly available catalogs:

1. the optical catalog in r, i, z bands (65,349 sources) obtained from observations with the Optical System for Imaging and low Resolution Integrated Spectroscopy (OSIRIS), mounted on the 10.4 m Gran Telescopio CANARIAS (GTC) of the Spanish Observatorio del Roque de los Muchachos in La Palma (Cepa et al. 2000) compiled by Guarcello et al. (2012);
2. the second release of the optical catalog in r', i', $H\alpha$ bands (24,072 sources) obtained from observations with the Wide Field Camera (WFC) on the 2.5 m Isaac Newton Telescope (INT) for the INT Photometric Hα Survey (IPHAS; Drew et al. 2005; Barentsen et al. 2014);
3. the SDSS catalog (eighth data release, DR8, 27,531 sources; Aihara et al. 2011) in u, g, r, i, z bands;
4. the UKIDSS/GPS catalog in the JHK bands (Hewett et al. 2006; Lucas et al. 2008), containing 273,473 sources, from observations taken with the Wide Field Camera (WFCAM; Casali et al. 2007) on the United Kingdom InfraRed Telescope (UKIRT), compiled adopting a new photometric procedure (King et al. 2013) based on the UKIDSS images (Dye et al. 2006);

5. the 2MASS/PSC catalog in *JHK* (Cutri et al. 2003; 43,485 sources); and
6. the catalog in the Spitzer/IRAC 3.6, 4.5, 5.8, and 8.0 μm and MIPS 24 μm bands (149,381 sources) from the Spitzer Legacy Survey of the Cygnus X region Spitzer (Beerer et al. 2010).

As described in Guarcello et al. (2013), these catalogs have been combined into a large OIR catalog containing 329,514 sources. The matching procedure was divided into three steps. First, a combined optical catalog was produced by matching the OSIRIS, IPHAS, and SDSS catalogs. Second, an infrared catalog was created by matching UKIDSS, 2MASS, and Spitzer data. In the last step, the two catalogs were merged into a unique OIR catalog. All the data used here, except those from OSIRIS, are available over the entire area surveyed with Chandra/ACIS-I. The OSIRIS data are only available in a central $40' \times 40'$ field.

The OIR catalog includes stars associated with Cyg OB2 down to very low masses. Assuming a distance of 1.4 ± 0.08 kpc (Rygl et al. 2012) and an average extinction $A_V = 4.3$ (Guarcello et al. 2012) and adopting the isochrones of Siess et al. (2000), we can estimate that we have good-quality optical and infrared data for members down to 0.2 $M_\odot$, allowing us an unprecedentedly deep and complete study of the population of Cyg OB2.

4. The Adopted Matching Procedures

The X-ray sources in our survey need to be classified also according to their OIR properties (Kashyap et al. 2023). Erroneous matches between the OIR and X-ray catalogs will result in wrong classifications, affecting the scientific outcome of our survey. For this reason, particular attention must be given to how the OIR and X-ray catalogs are merged.

A simple matching procedure based on the positions of the sources and using a fixed matching radius (i.e., considering as real counterparts the OIR and X-ray pairs with a separation smaller than a given threshold) is unsuitable to our case for two reasons. First, the point-spread function (PSF) of the Chandra mirrors increases in size with increasing off-axis angle. For this reason, the positional accuracy of the X-ray sources is not constant across the field. Second, while the optical data are dominated by the foreground stellar population and the infrared data are dominated by the background sources, in both cases with an approximately uniform spatial distribution, most of the X-ray sources with OIR counterparts are expected to be associated with Cyg OB2 and clustered at the locations of the various subclusters of the association. The density of the sources not associated with the X-ray population (the uncorrelated population) is high, and any attempt at matching the OIR and X-ray catalogs using only positional information will inevitably result in large numbers of spurious matches. It is necessary, then, to use a more sophisticated approach.

One method used successfully in similarly challenging matching procedures is based on ML (Sutherland & Saunders 1992) approaches and takes into account both the spatial separation between the different catalog sources (OIR and X-ray in our case) and how the magnitude of the OIR sources compare with those expected for the real OIR counterparts of the X-ray sources (the correlated population). Several ML methods have been used in the literature (i.e., Taylor et al. 2005; Gilmour et al. 2007; Rumbaugh et al. 2012). In this work, rather than rely on a single matching procedure, we adopt three different methods. The final OIR–X-ray catalog will contain all the pairs matched with each of the three methods, with the subsample of the most reliable matches properly tagged.

4.1. Modified Smith et al. (2011) Procedure

One of the methods that we adopted is defined in Smith et al. (2011), slightly modified in order to optimize it for our specific multiwavelength case. In this approach, the probability that a given OIR source is the correct counterpart of a nearby X-ray source is calculated starting from the following likelihood ratio:

$$LR = \frac{q(m)f(r)}{n(m)}. \tag{1}$$

In this definition, $f(r)$ is the radial distribution function of the separations between OIR and X-ray pairs as a function of the positional error:

$$f(r) = \frac{1}{2\pi\sigma_{\rm pos}^2}\exp\left(\frac{-r^2}{2\sigma_{\rm pos}^2}\right). \tag{2}$$

Here r is the positional offset between OIR and X-ray sources and $\sigma_{\rm pos}$ are the positional uncertainties, calculated adding in quadrature the OIR and X-ray positional uncertainty. The quantities $q(m)$ and $n(m)$, i.e., the magnitude probability distributions of the correlated OIR sources and the observed magnitude probability distribution of all the OIR sources in the m band, respectively, are described in the next sections.

4.1.1. The Observed Magnitude Distributions

In Equation (1) $q(m)$ and $n(m)$ are the probabilities to observe, respectively, a correlated and a generic OIR source with magnitude m. The main difference between the method we used and that defined in Smith et al. (2011) is that the latter method is applied using one optical catalog. Our multiwavelength catalog contains data from various optical and infrared catalogs, and most of the sources lack a detection in one or more of them. For instance, highly embedded or extinguished objects in the background, or even associated with the most obscured regions of Cyg OB2, often lack optical counterparts.

For this reason, we seek to use all the OIR information available in order to improve the completeness of the final OIR +X-ray catalog. We calculated, then, $q(m)$ and $n(m)$ for each band available in our OIR catalog. We also defined for each OIR source a representative band, which is the first one available and with an error smaller than 0.1 mag proceeding from shorter to longer wavelengths, starting from the r band. In the optical bands we used preferentially the OSIRIS photometry. The IPHAS photometry has been used when OSIRIS data are not available, and SDSS photometry has been used when there are no other optical data. Our main catalog in the near-infrared is UKIDSS, while 2MASS data are used when UKIDSS data are not available or of bad quality. This priority among the available bands has been arbitrarily chosen, after having verified that the chosen order was not affecting our results, since it was possible to define a representative band for almost all the bands. For the vast majority of sources in our OIR catalog, the representative bands are the OSIRIS r or the UKIDSS J bands.

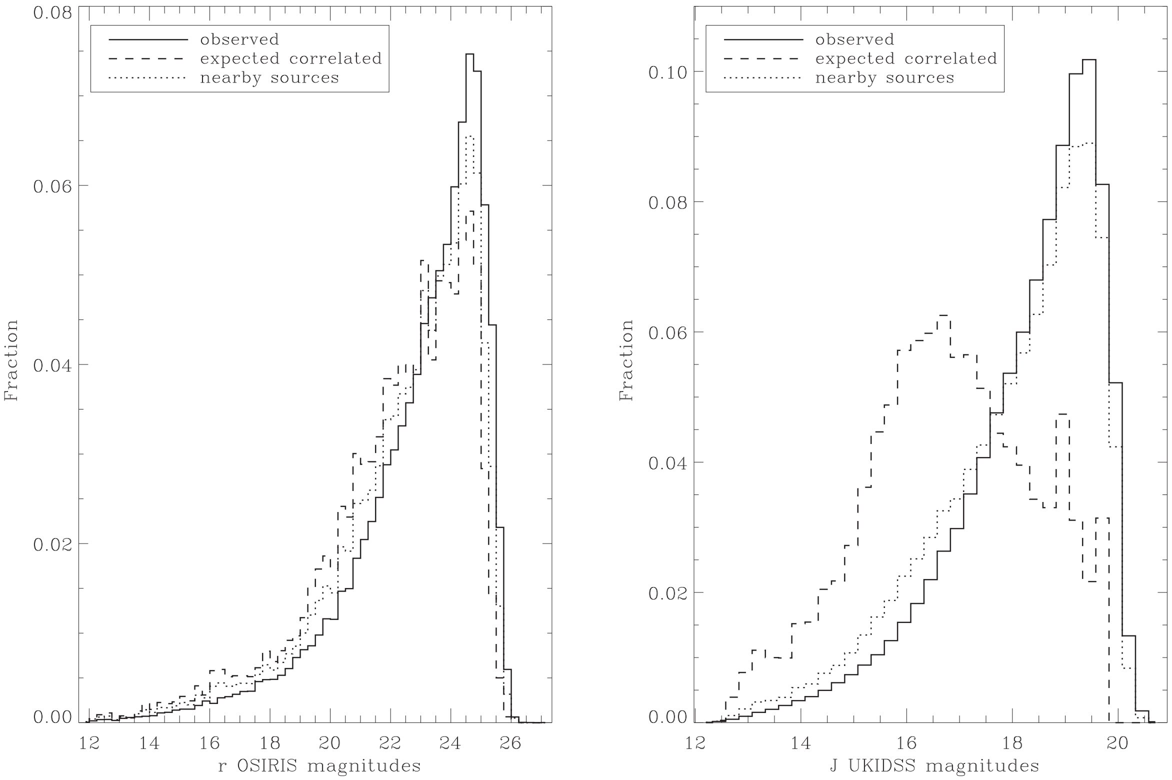

Figure 1. Magnitude distributions in the OSIRIS r (left panel) and UKIDSS J (right panel) bands for the entire OIR catalog (solid histogram), the nearby sources (dotted histogram), and the expected correlated distributions (dashed histograms) using Equation (3) (SM method).

To obtain $n(m)$, we first calculated the observed magnitude distributions in each band of our catalog, sampled in bins of 0.25 mag of width. The probability $n(m)$ for a given OIR source is then given by the fraction of sources observed in our OIR catalog in the representative band in the same magnitude bin, normalized by the total area of the survey.

4.1.2. The Correlated Magnitude Distributions

The calculation of $q(m)$ for each OIR source is more complicated, since it requires the computation of the magnitude distribution of the expected correlated population, after considering and removing the contribution from the uncorrelated population. Following Smith et al. (2011), the initial approximation of the expected magnitude distribution of the correlated population is obtained from all the OIR sources closer than 10″ to the X-ray sources (hereafter the nearby population). Even at large off-axis angles, this matching radius is significantly larger than the propagated positional uncertainty, resulting in a selection of 78,182 nearby OIR sources for the 7924 X-ray sources. The expected magnitude distribution of the correlated population is obtained from that of the nearby population, by subtracting in each magnitude bin the number of uncorrelated sources expected to match the positions of the X-ray sources and falling in the given bin of magnitude:

$$q(m) = \text{nearby}(m) - N(m) \times N_x \times \frac{\Delta_{\text{match}}}{\Delta_{\text{tot}}}, \tag{3}$$

where nearby(m) is the magnitude distribution of the nearby sources, N_x is the total number of X-ray sources (7924), Δ_{match} is the matching area with a radius of 10″, Δ_{tot} is the total area of our survey (1 deg^2), and $N(m)$ is the observed magnitude distribution $n(m) \times \Delta_{\text{tot}}$. By using this formula, we are also assuming that the uncorrelated sources are uniformly distributed in the survey area, which may be incorrect in case of nonuniform extinction such as in Cyg OB2.

Figure 1 shows the magnitude distributions in the OSIRIS r and UKIDSS J bands for the entire OIR catalog, the nearby sources, and the expected correlated population. In the optical band there is not much difference between these distributions, not even in the faint part. This may indicate that this method is not very effective in removing fortuitous coincidences between X-ray sources and faint background optical sources. The correction used to remove the uncorrelated population has been more effective in the J band, as demonstrated by the difference between the total distribution, centered at $J = 19.5$, and the expected correlated distribution, centered in the range $16 < J < 17$.

4.1.3. Reliability Associated with an OIR+X-Ray Pair

Once we have calculated $f(r)$, $q(m)$, and $n(m)$, we can obtain LR for each pair of X-ray and OIR sources from Equation (1). Using the value of LR, we can assign a probability that a given OIR source is the real counterpart of the nearby X-ray source and compare it with a chosen threshold (see Section 4.1.4). This probability is calculated comparing the observed LR value with a distribution of LR values obtained from 200,000 test X-ray sources uniformly distributed across the field. The use of uniform spatial distribution of the X-ray sources is an acceptable approximation since the OIR catalog, dominated by background NIR sources, has a nearly uniform spatial density. These test sources were matched with the OIR catalog, obtaining a distribution of simulated LR values from more than 70,000 pairs (the exponential form in $f(r)$ cuts any match between sources more distant than a few arcseconds).

The reliability associated with each match between the X-ray and OIR sources in our catalog, which is, by definition, the probability that the given OIR source is the real counterpart of the nearby X-ray source, is then calculated as

$$R_{ij} = 1 - \frac{N_{gt}}{N_{\mathrm{sim}}}, \tag{4}$$

where R_{ij} is the reliability that the OIR source i is the real counterpart of the X-ray source j, N_{sim} is the number of simulated LR values, and N_{gt} is the number of simulated LR values larger than the one observed between the ij pair

$$N_{gt} = N(LR_{\mathrm{simul}} > LR_{ij}). \tag{5}$$

In this way each ij pair (i.e., each pair of X-ray and OIR sources) has an associated probability that the OIR source is the real counterpart of the X-ray source.

4.1.4. Match Results

The last step consists in assigning a probability cutoff, i.e., to decide what is the minimum reliability that identifies real matches. This was performed by studying how the number of spurious matches out of the total number of matches increases with decreasing the cutoff. To obtain the number of spurious matches, we repeated the matching procedure after "randomizing" our X-ray catalog, i.e., applying rigid translations of 1′ to the X-ray sources four times, each time with a different combination of positive and negative rigid translations in R.A. and decl. The number of expected spurious matches corresponding to given test values of the cutoff is the mean of the number of matches obtained with these four "randomized" X-ray catalogs. We then fixed our cutoff value as the one for which the ratio of spurious to total matches is ∼10% (corresponding to $R_{\mathrm{cutoff}} = 0.95$).

Figure 2 shows how the numbers of total and spurious matches, together with their ratio, vary with the test thresholds. With the chosen cutoff of 0.95, we matched 5180 pairs, with 4946 single matches. Hereafter this method is called the SM method.

4.2. Matching Procedure with the Correlated Population from an Accurate Position Match

The second matching procedure is based on a different definition of the correlated population. The definitions of LR (Equation (1)), of the observed magnitude distributions $n(m)$, and of the reliability (Equations (4) and (5)) and the procedure to define the threshold (Section 4.1.4) are the same as those adopted in the previous sections.

In Section 4.1.2 we calculated the magnitude distribution of the expected correlated population starting from a position match between the X-ray and OIR catalog with a large matching radius (10″), and then we used a statistical approach to remove from the nearby population the expected contribution of the uncorrelated OIR sources. This correction was necessary, as proved by the very large number of nearby sources found (78,182) and the risk that the SM method may not be very effective in removing spurious coincidences between X-ray and faint optical sources in the background. However, since the chances that OIR sources nearby X-ray positions are real counterparts decrease with increasing separation, a different estimate of the correlated population can be found with a nearest neighbor match using suitable small matching radii estimated with a detailed statistical analysis of real and spurious matches.

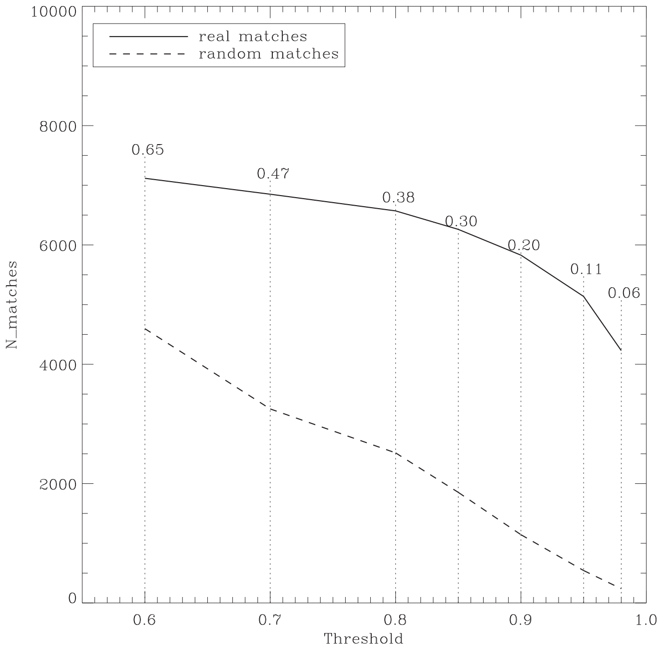

Figure 2. Number of real (solid line) and spurious (dashed line) matches obtained with increasing the reliability threshold in the SM method. The numbers over the solid line show how the fraction of spurious matches decreases with increasing the threshold.

4.2.1. The Correlated Population from Accurate Nearest Neighbor Match

In this procedure, we obtained a correlated population from which we derived $q(m)$ from an accurate nearest neighbor match. The matching radius used in this procedure must take into account the degradation of the PSF in the X-ray images at increasing off-axis angles and the photon statistics of the X-ray source. In order to do that, we used an individual matching radius for each X-ray source that is proportional to the X-ray positional uncertainty, the latter calculated as in Kim et al. (2007):

$$r_{\mathrm{match}} = A \times \sigma_{\mathrm{pos}} \tag{6}$$

$$\log(\sigma_{\mathrm{pos}}) = 0.1137\Theta - 0.46\log(C) - 0.2398 \tag{7}$$

$$\log(\sigma_{\mathrm{pos}}) = 0.1031\Theta - 0.1945\log(C) - 0.8034, \tag{8}$$

where r_{match} is the individual matching radius, A is a coefficient to be evaluated, σ_{pos} is the positional uncertainty, Θ is the off-axis angle of the X-ray sources, and C is the net number of counts. Following Kim et al. (2007), Equation (7) is applied to sources with less than 133 counts; Equation (8) is applied to brighter sources.

Given the different depth and spatial distribution of the optical, *JHK* (UKIDSS and 2MASS), and Spitzer catalogs, we decided to perform the nearest neighbor match for each of these three catalogs separately and then to merge the results. The crucial step here is to estimate the coefficients A for the three catalogs, together with a minimum allowed matching radius (r_{min}). The use of r_{min} is necessary since the positional errors in the center of the ACIS field are very small, resulting in unacceptably low matching radii.

Table 1
Results of the Close-neighbor Matches

OIR Catalog	$r_{\rm min}$	A	No. Matches
Optical	0.″6	1.4	4917
JHK	0.″5	0.9	5025
Spitzer	0.″5	1.3	5278

The procedure adopted to calculate these parameters is similar to that defined in Section 4.1.4, i.e., by comparing the ratio of the numbers of spurious coincidences to that of the total matches obtained with increasing test values of A and $r_{\rm min}$. The spurious coincidences are calculated by matching the OIR catalogs with "randomized" X-ray catalogs (as in Section 4.1.4), while the total number of matches is calculated by combining the OIR catalogs with the "real" X-ray catalog (i.e., with no positional offset added). We first evaluated A and then $r_{\rm min}$, in both cases as the largest test values at which the spurious matches reached ∼10% of the real matches. Table 1 lists the values of A and $r_{\rm min}$ found for the optical, *JHK*, and *Spitzer* catalogs, together with the total number of matches. The catalog of the expected *correlated* sources obtained by merging the results of these three nearest neighbor matches numbers 5820 sources, many less than the *nearby sources* defined in Section 4.1.2 and comparable to the final number of the OIR +X-ray pairs matched in the merged catalog (Section 5). This catalog has been used to define the magnitude distribution $q(m)$ used in Equation (1).

Figure 3 shows the distributions of the OSIRIS r and UKIDSS J magnitudes for all the OIR sources and for the expected correlated population found with the accurate nearest neighbor match described here. Comparison with Figure 1 reveals that the magnitude distributions obtained with this method are shifted for brighter magnitudes: the r distribution of the correlated population in Figure 3 is centered in the range $20 < r < 22$, while in Figure 1 it is peaked at about $r \sim 24$ similar to the distribution of the total OIR catalog. The effect in the J distribution is smaller. This indicates that this method is more effective than the SM method in removing candidate spurious matches with faint sources.

The rest of the procedure (i.e., the calculation of the reliability and the threshold for reliable matches, equal to 0.96) was performed as described in Sections 4.1.3 and 4.1.4 and resulted in 5210 matches (4933 single matches). Hereafter this method is called the PM method.

4.3. Naylor et al. (2013) Bayesian Method

A Bayesian technique to cross-correlate X-ray catalogs with deep infrared data has been developed by Naylor et al. (2013), as an extension of the techniques defined in Sutherland & Saunders (1992). This method has several similarities with the ML methods described above. As in those methods, the magnitude of the candidate OIR counterpart is compared with an expected magnitude distribution for the correlated population to reduce the chances of matching the X-ray sources with an uncorrelated background or foreground source.

We defer a description of the method to Naylor et al. (2013), although note that it brings two significant improvements to existing match criteria such as those we used to define our ML methods. First, it has a more sophisticated method of estimating the magnitude distribution of the correlated population, which allows for the fact that the presence of counterparts in the error circles means that they are more crowded than the field. The second improvement lies in accounting simultaneously for all the OIR sources close to an X-ray position to calculate the probability that each of them is the real counterpart of an X-ray source. This is not the case with the methods described above, where the reliability is calculated independently from the values obtained for the other nearby OIR sources. The main gain of the more sophisticated approach is in reducing chances of multiple source matches.

We applied the method using the i-band, K-band, and [3.6] photometry, where the number of available sources with good photometry is larger, merging the various catalogs available for each band using the hierarchy described in Section 4.1.1. Since the matching method requires a magnitude for each star, we removed from the catalog all objects that did not have magnitudes in the band in question, or had a magnitude whose uncertainty was greater than 0.3.

The first stage of the matching process is to check the model of the X-ray error circles by comparing the distribution of stars around all the X-ray positions with that predicted by a model consisting of a uniform background and a set of counterparts. The latter were initially assumed to have a Gaussian distribution about the X-ray positions with the radius given by the Kim et al. (2007) model. We found that the data were best fitted by multiplying the radius of the error circles by 0.6 and adding in quadrature a position- and X-ray-flux-independent uncertainty of 0.″2. The combination suggests that the Kim et al. (2007) radii overestimate the positional uncertainty in our data by perhaps 20%. We also explored systematic offsets in the data and found that the best fit corresponded to a shift in R.A. of 0.″02 with no shift in decl.

The remainder of the matching process proceeded as described in Naylor et al. (2013) and resulted in a list of all stars that had a likelihood of being a counterpart greater than 0.05. The counterpart probabilities are presented along with those from the other methods in our final catalog. We included in the list of counterparts only those stars whose likelihoods exceeded 0.8. We can estimate the contamination in this sample by summing all the likelihoods that a given star is not the counterpart and then dividing this by the number of counterparts. For both the K- and i-band samples with likelihoods greater than 0.8 this gives a contamination rate of about 2%.

The total number of sources matched with this method is 5157. Considering only the single matches, the number of sources matched by this method is similar to those matched by the two ML methods: 4933 sources with the PM method, 4946 with SM, and finally 4958 with this method, called hereafter the NBF method.

5. The Final OIR+X-Ray Catalog

5.1. Most Reliable Matches

The catalog merged from all the above methods numbers 5703 OIR+X-ray pairs matched with at least one method: 4643 are matched with all three methods, 558 with two, and 502 with just one. Among the matched sources, there are 5398 single matches and 305 multiple matches. Figure 4 shows the r versus $r - i$ diagram of all the optical sources with good photometry within the Chandra Cygnus OB2 Legacy field. The conditions for good photometry are defined in Guarcello et al. (2012): in short, they require small errors ($\sigma_r < 0.1$ and

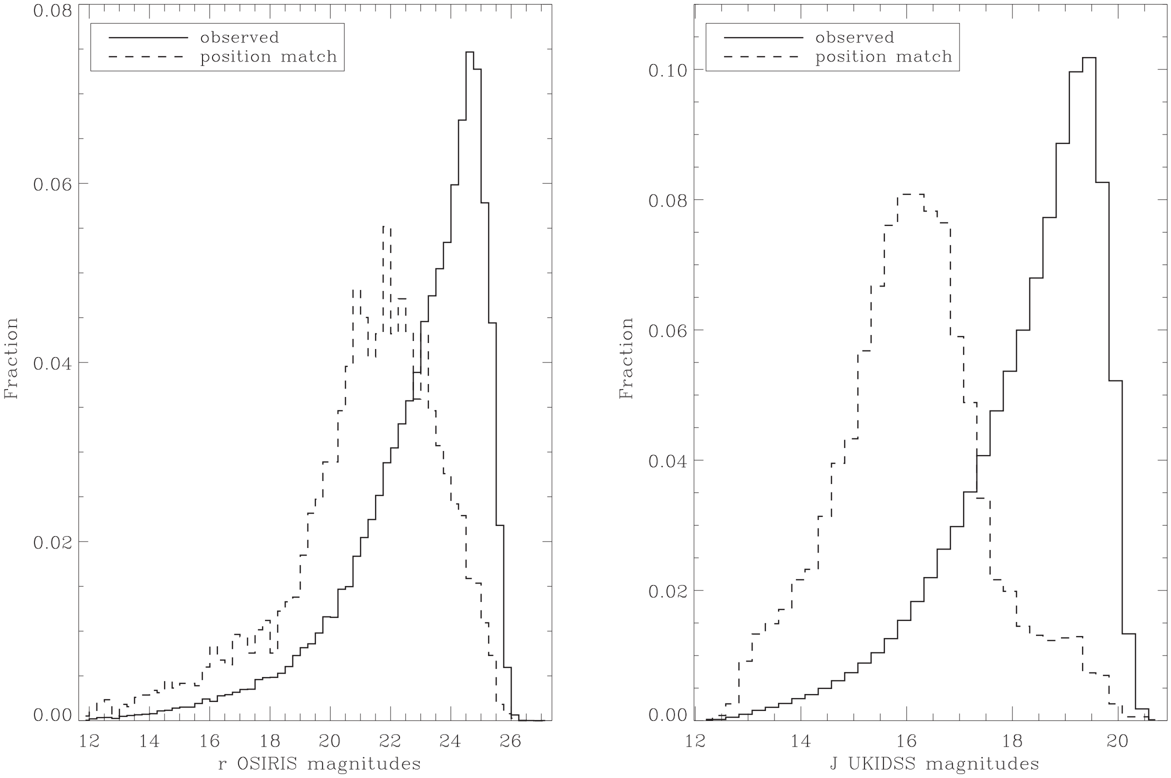

Figure 3. Magnitude distributions in the OSIRIS *r* (left panel) and UKIDSS *J* (right panel) bands for the entire OIR catalog (solid histogram) and for the OIR sources matched with the X-ray sources using an individual matching radius as described in Section 4.2.1, i.e., in the PM method (dashed histogram).

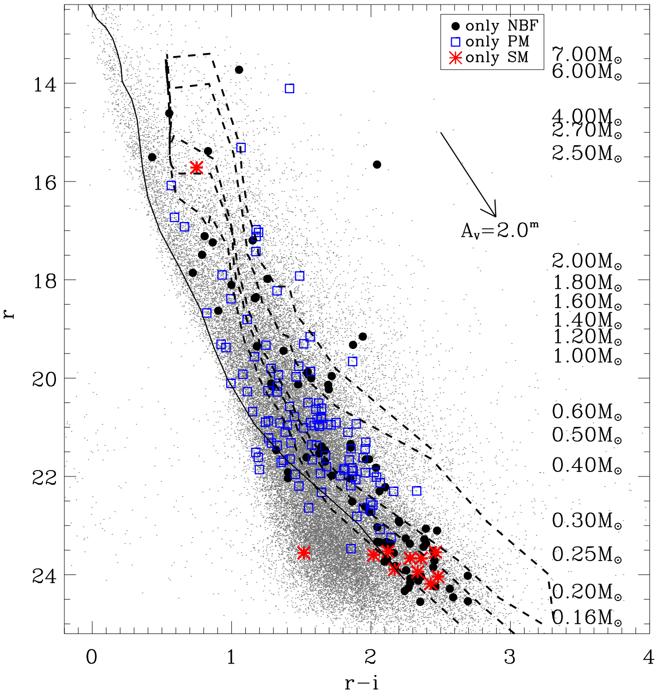

Figure 4. The r vs. $r-i$ diagrams, with all the sources with good optical photometry marked with gray dots, the isochrones with age <10 Myr, and the ZAMS plotted using the distance and extinction as in Guarcello et al. (2012). The reddening vector and the masses corresponding to the 3.5 Myr isochrone are also shown. Different symbols and colors mark the X-ray sources matched with just one method.

$\sigma_{r-i} < 0.15$) in at least one of the three optical catalogs we have used. Also shown in Figure 4 are the isochrones and zero-age main sequence (ZAMS) from Siess et al. (2000), plotted using a distance of 1.4 ± 0.08 kpc (Rygl et al. 2012), with the extinction $A_V = 4.3$ for the isochrones and $A_V = 1$ for the ZAMS (Guarcello et al. 2012). On the right side of the diagram are marked the r magnitudes of 3.5 Myr old stars with $A_V = 4.3$ and $d = 1.4 \pm 0.08$ kpc with different masses. The extinction vector is obtained from the extinction law of O'Donnell (1994). The sources matched with only one method are overplotted with different symbols and colors, as explained in the legend. The sources matched only with the NBF method lie mainly in the cluster locus (i.e., in this diagram the area between the isochrones), spanning the entire magnitude range but with a larger fraction of faint sources. Following the reddening vector, these sources can be stars associated with Cyg OB2 suffering large extinction, or low-mass members observed during a period of high X-ray activity. The analysis of their X-ray spectra and light curves will help us to better classify them (Flaccomio et al. 2023). The sources matched only with the PM method populate mainly the region of the diagram with intermediate magnitudes. Most of them are compatible with the cluster locus. The sources matched only with the SM method lie only in the faint end of the cluster locus. The fact that all the sources matched only by the SM method are faint is likely a consequence of the lower effectiveness of the SM method in removing spurious matches with faint optical uncorrelated sources (Figure 1). These samples show the same properties in all the optical and infrared color–magnitude diagrams.

Figure 5 shows the J magnitudes of the OIR counterparts of the matched sources versus their separation from the X-ray sources, for the pairs matched only with the NBF method and those matched only with the ML methods. In this diagram the differences between these two samples are evident: the stars matched only with the NBF method are systematically fainter and closer, indicating that the ML methods (mainly PM) have

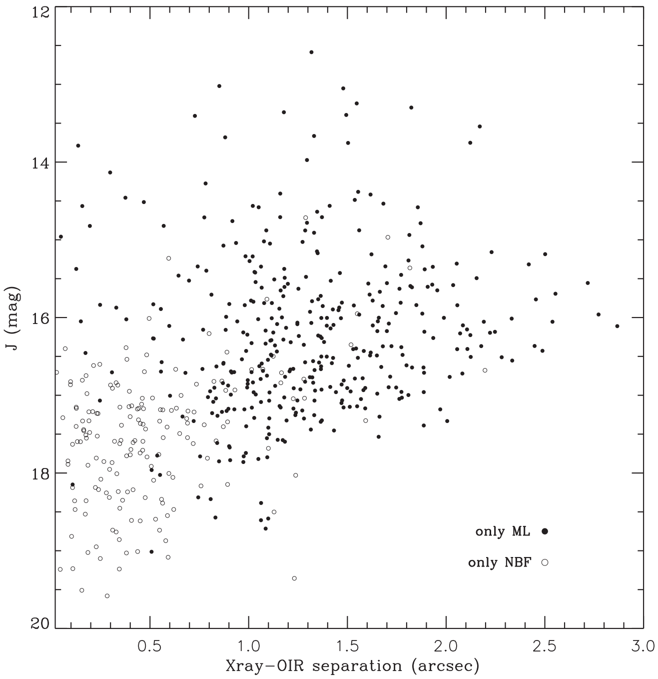

Figure 5. J magnitude of the OIR counterparts vs. the separation between the OIR and the X-ray counterparts for the sources matched only with the NBF or the ML methods.

been very conservative in removing candidate spurious coincidences with close faint counterparts. On the other hand, the ML methods are more effective in matching OIR counterparts with intermediate and bright magnitudes and at large separations (i.e., larger than 1″), which are plausible given the size of the ACIS PSF.

The merged OIR and X-ray catalog is described in Appendix. As explained earlier, the 305 multiple matches are kept in the merged catalog. Different scientific uses of the catalog require different treatment of the multiple matches. For instance, studies based on stellar positions may simply consider the multiple matches as a single entry at a given position, or studies based on the photometric properties would require us to discard the multiple matches. For those cases where one of the matching counterparts in the multiple matches must be chosen, we provide in the catalog a column indicating the "best counterpart." Users must use this column and deal with multiple matches with caution. Given the evidence that the SM method is not efficient in removing spurious coincidences between the X-ray and faint optical sources and the fact that the expected magnitude distribution of the correlated stellar population is calculated with a statistical approach that is not fully suitable for our survey, we consider as "most reliable matches" the 5619 sources matched by either the NBF (the NBF sample) or PM (the ML sample, i.e., removing the sources matched only by the SM method) method.

5.2. Properties of the X-Ray+OIR Sources

Guarcello et al. (2013) studied the disk population of Cyg OB2 within the field of the Chandra Cygnus OB2 Legacy Survey. They selected and classified 1843 stars with disks associated with Cyg OB2. Among these stars, a total of 444 have an X-ray counterpart: 368 class II sources, 10 candidates with transition disks, and 19 with pre-transition disks; 20 candidate accretors with intense Hα emission; 6 blue stars with disks (Guarcello et al. 2010); and 16 candidate class I sources.

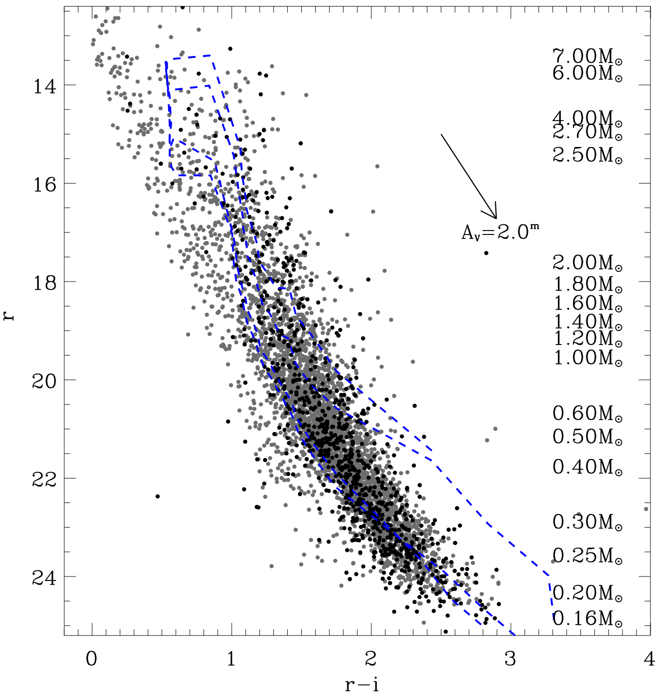

Figure 6. The r vs. $r-i$ diagrams, with all the X-ray sources with a "reliable" OIR counterpart with good optical photometry marked with gray dots, and with the Cyg OB2 members with circumstellar disks marked with black dots. The isochrones, reddening vector, and masses are plotted as in Figure 4.

We also detected the X-ray emission from 52 known O stars, 57 known B stars, and 6 emission-line objects selected by Vink et al. (2008). Other existing classifications of low-mass members of Cyg OB2 made use of X-ray observations that are part of the Chandra Cygnus OB2 Legacy Project (Albacete Colombo et al. 2007; Wright & Drake 2009), so that they are included in the list of candidate members produced by our survey. Figure 6 shows the r versus $r-i$ diagram of the optical counterpart of the X-ray sources with "reliable" OIR matches. Their locus in this diagram is well delimited by the chosen isochrones, which correspond to the locus of the candidate members with circumstellar disks selected by Guarcello et al. (2013). This suggests that this sample is dominated by young stars associated with Cyg OB2. Optical−X-ray counterpart and disk-bearing sources show a slightly different distribution in r, with the former being more numerous at bright magnitudes. This can be understood as a consequence of the fact that (1) low-mass stars hold their inner disks for a longer time than high-mass stars, (2) the X-ray catalog is not complete below 1 $M_\odot$ (Wright et al. 2023b), and (3) the bright end of the r distribution is more populated by candidate foreground stars detected in X-rays. For instance, a significant population of field stars apparently older than Cyg OB2 stars lies in the bright blue part of the diagram (i.e., $r \leqslant 15.5$ and $r-i \leqslant 0.4$). These stars have an extinction significantly smaller than that of the Cyg OB2 stars, as inferred from other color–color diagrams.

Figures 7 and 8 show several optical and infrared color–color diagrams of the OIR sources with X-ray counterparts (black dots) classified as "most reliable matches," together with all the sources meeting the criteria for good photometry in the relevant bands (i.e., errors in colors smaller than 0.15 mag). In the $r-i$ versus $i-z$ diagram most of the X-ray sources with optical counterparts lie in the area delimited by the 3.5 Myr isochrones from Siess et al. (2000) with extinction $A_V = 2.6$

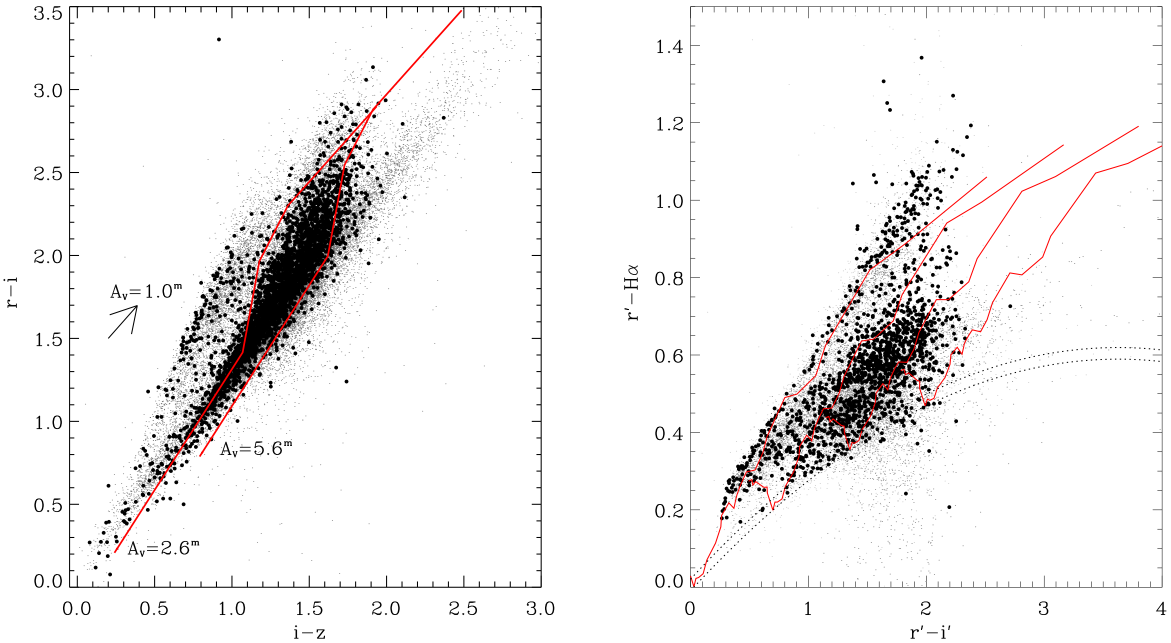

Figure 7. Optical color–color diagrams with all the sources with good photometry in the involved colors (gray dots) and the "most reliable" counterparts of X-ray sources (black dots). In the $r - i$ vs. $i - z$ diagram the solid lines are 3.5 Myr isochrones with $A_V = 2.6$ and $A_V = 5.6$; in the $r' - \mathrm{H}\alpha$ vs. $r' - i'$ diagram the solid lines are ZAMS with increasing E_{B-V} from 0 to 4.

and $A_V = 5.6$, which are the 10% and 90% quantiles, respectively, of the optical extinction found in Guarcello et al. (2012). The optical+X-ray sources to the left of the less extinguished isochrone are likely foreground sources, while possible background sources cannot be distinguished from the faintest stars associated with Cyg OB2. These properties are only weakly dependent on the isochrones used.

Another diagram where the foreground population can be easily distinguished from Cyg OB2 members is the $r' - \mathrm{H}\alpha$ versus $r' - i'$ diagram. The solid lines are the ZAMS from Drew et al. (2005) with $E_{B-V} = 0$, 1, 2, 3. The X-ray sources that lie close to the $E_{B-V} = 0$ ZAMS are mainly in the foreground. Other classes of sources that can be distinguished are the background giants that mainly lie in the lower part of the diagram, below the ZAMS (Wright et al. 2008), and accreting stars that show very red $r - \mathrm{H}\alpha$ colors. Only a handful of IPHAS+X-ray sources lie in this part of the diagram. Moreover, candidate A stars are expected to populate the locus in this diagram within the dashed curved lines (Drew et al. 2008).

The loci shown in the three infrared diagrams in Figure 8 (i.e., the Giants, Disk, and Galaxies loci) have been defined in Guarcello et al. (2013). In the $J - H$ versus $H - K$ diagram only a few NIR+X-ray sources lie in the *disk* locus or at very high extinction. The first result is not surprising, since only 7.5% of the selected stars with disks in Cyg OB2 populate this locus (Guarcello et al. 2013); the second result suggests that the background contamination of the X-ray sources with NIR counterparts is low. Very small contamination from galaxies is also suggested by the $[3.6] - [5.8]$ versus $[4.5] - [8.0]$ diagram, which is one of the diagrams used in Guarcello et al. (2013) for selecting disks and galaxies. In this diagram, the X-ray sources with IR excesses due to the presence of a circumstellar disk lie inside and nearby the disk locus in the upper right part. Most of the X-ray sources with MIPS counterparts have intrinsic red colors, likely due to circumstellar disks, as shown in the $[4.5] - [5.8]$ versus $[5.8] - [24]$ diagram. In all the discussed diagrams, the reddening vectors are taken from the extinction laws found by Rieke & Lebofsky (1985), O'Donnell (1994), and Flaherty et al. (2007).

In Figure 9 we show the spatial distribution of all the X-ray sources with OIR counterparts, which are clearly clustered in the center of the field that roughly corresponds to the central cluster of Cyg OB2 (Bica et al. 2003; Guarcello et al. 2013), but there is also a rich sparse population across the entire field. The contours mark the emission at 8.0 μm, showing the locations of the densest nebular structures.

The analysis of the X-ray properties of the X-ray sources with an OIR counterpart is beyond the scope of this paper, and it will be part of dedicated studies (Flaccomio et al. 2023; Kashyap et al. 2023). A brief comparison of the observed X-ray photons' energy between the X-ray sources with and without an OIR counterpart is shown in the next section.

5.3. Properties of the Unmatched X-Ray Sources

The different nature of the X-ray sources with and without OIR counterparts is evident by comparing their spatial distribution and their median photon energy, shown in Figures 10 and 11. The distribution of the X-ray sources with OIR counterpart is peaked at about 1.65 ± 0.15 keV. The distribution of the X-ray sources with no OIR counterpart is completely different, being flatter, shifted toward higher energies and approximately bimodal, with a high-energy cutoff at about 3.45 ± 0.15 keV. The two distributions can be understood if the former is dominated by stars associated with Cyg OB2, while the latter is dominated by background and extragalactic sources, mainly active galactic nuclei, with also a small presence of possible less extinguished stars. The right panels show the distributions of the net counts for the two samples of X-ray sources. An evident excess of faint X-ray sources is observed among the X-ray sources with no OIR counterpart compared to those with a counterpart.

Comparing the spatial distribution of the unmatched X-ray sources (Figure 10) with that of the OIR+X-ray stars (bottom

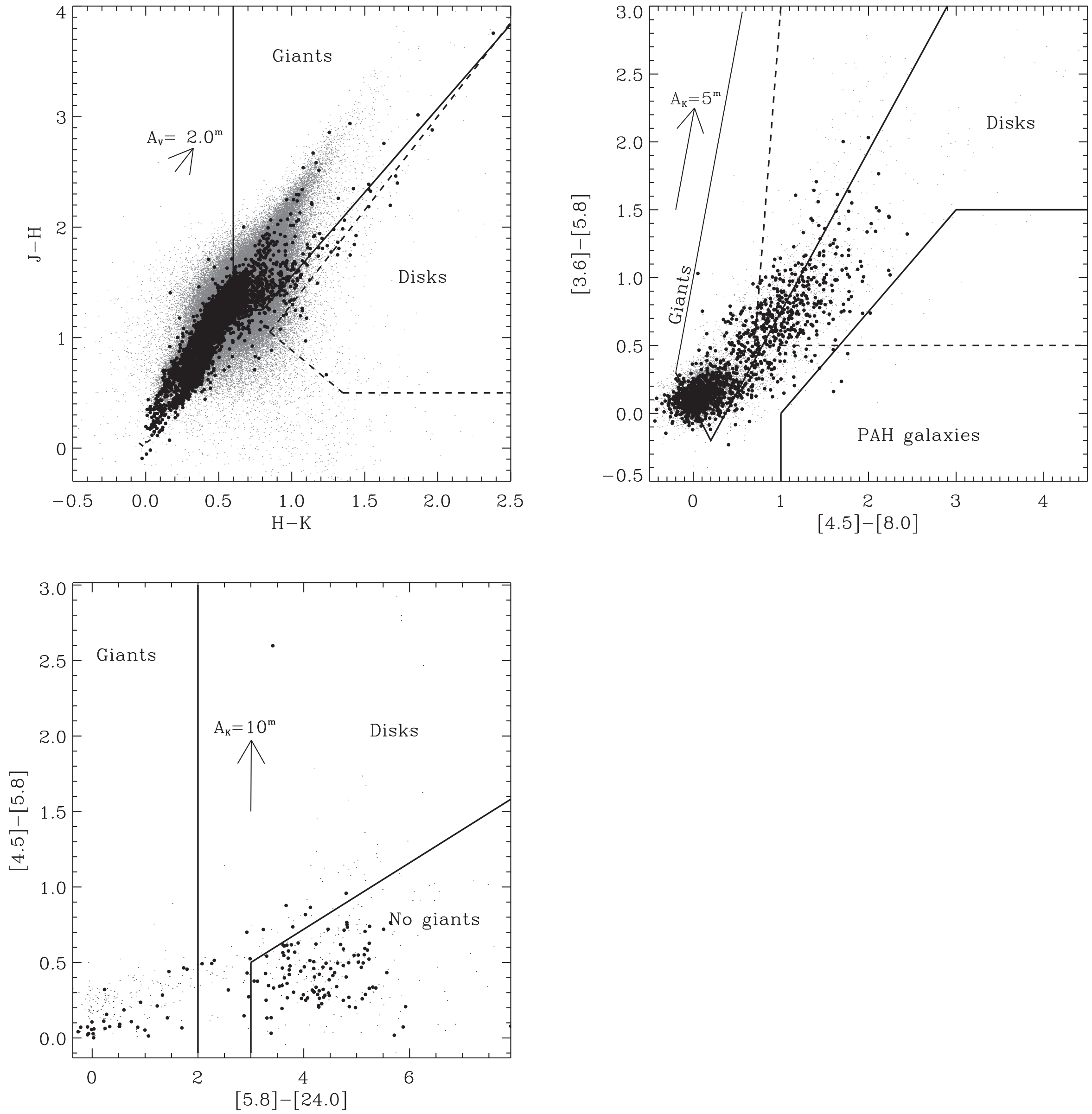

Figure 8. NIR color–color diagrams with all the sources with good photometry in the involved colors (gray dots) and the "most reliable" counterparts of X-ray sources (black dots). The loci shown in the diagrams distinguish the typical colors expected from giants and normal stars at various extinctions, disk-bearing stars, and background galaxies. In the right panel, giants can be found across the entire diagram, except for the locus marked with "No giants."

right panel of Figure 9), it is evident that the latter show a high degree of clustering in the center of the field, as expected, while the former are almost uniformly distributed. For instance, in the central area, within 8′ from the median position of all the X-ray sources, fall 24% of the X-ray+OIR sources, and only 13% of the X-ray sources with no OIR counterpart. In Figure 10 we do not observe a strong concentration of sources toward the densest nebular structures, suggesting that the number of very extinguished members of Cyg OB2 among the unmatched X-ray sources is low. We expect that a significant number of spurious X-ray detections are in the area around Cyg X-3, approximately at the position marked as "X-3" in Figure 10.

Figure 12 shows the diagram of the *J* magnitudes of the closest OIR sources to each unmatched X-ray source versus their angular separation. As expected, the distribution of sources in this diagram is almost complementary to those in Figure 5. The vast majority of the sources here have large separations, with the exception of 206 X-ray sources with an OIR source closer than 1″. Of these, 143 are faint in *J* (having $J > 18$), and only 18 have a brighter *J*. For 45 of these sources the *J* photometry is absent or of poor quality.

6. Conclusions

In this paper we compile a catalog of X-ray sources with optical and infrared counterparts of the massive star-forming region Cyg OB2. The X-ray catalog is obtained from the 1.08 Ms Chandra Cygnus OB2 Legacy Survey, covering an area of 1 deg^2 centered on Cyg OB2. The X-ray catalog contains 7924 sources. The OIR catalogs have been compiled by merging several deep catalogs available for this region: from observations taken with OSIRIS@GTC (in *riz* bands), the public catalogs SDSS/DR8 (in *ugriz* bands), IPHAS/DR2 (in $r'i'\mathrm{H}\alpha$ bands), and UKIDSS/GPS and 2MASS/PSC (*JHK* bands), and from the Spitzer Legacy Survey of the Cygnus X region (in IRAC and

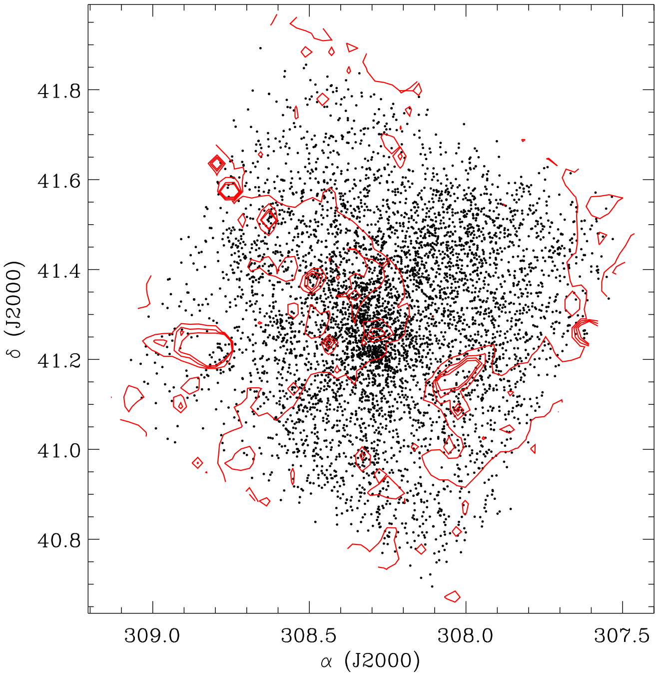

Figure 9. Spatial distribution of the X-ray sources with reliable OIR counterparts. The red solid lines mark the emission contours at 8.0 μm.

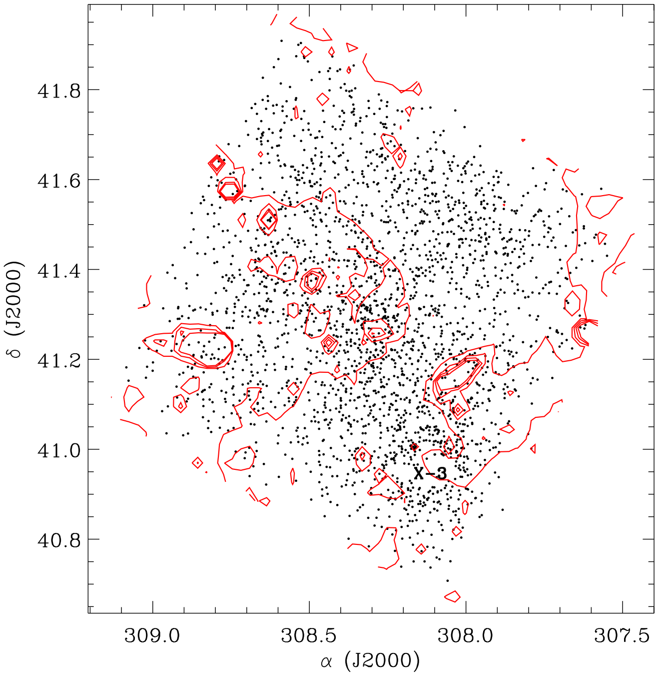

Figure 10. Spatial distribution of the X-ray sources without OIR counterparts, with the emission contours at 8.0 μm overplotted.

24.0 μm bands). This catalog contains 329,514 sources in the square degree area observed with Chandra/ACIS-I.

We discuss how a simple nearest neighbor match would result in a highly contaminated catalog, with an excess of false positives and spurious matches. To avoid this, we adopted three different matching procedures, two based on an ML approach plus the Bayesian method defined in Naylor et al. (2013). The two ML methods adopt different approaches to define the expected magnitude distribution of the real OIR counterpars of the X-ray sources. In one method this is obtained from a statistical approach from the observed magnitude distribution of the OIR source nearby the X-ray positions. In the other, it is obtained by using an accurate closest-neighbor match. All three methods have been used, and the results are merged in a single unique catalog. This merged catalog contains 5703 sources with X-ray and optical/infrared counterparts. We show that the most reliable OIR counterparts are found with the Bayesian method and the ML, which uses the closest-neighbor match to define the expected correlated magnitude distribution, counting 5619 matches. The nature of these sources is discussed using optical and infrared color–color and color–magnitude diagrams: the vast majority are compatible with being associated with Cyg OB2; a low contamination from candidate background galaxies and giant stars is observed, while the foreground population looks to be more significantly represented. Our combined catalog also contains 444 stars with disks, 52 O stars, and 57 B stars.

Acknowledgments

We thank the anonymous referee who helped us to improve the clarity of the manuscript. This paper is based on X-ray data obtained from the Chandra/ACIS-I observations of CygOB2, together with archival optical and infrared data. We made extensive use of the software provided by the Chandra X-ray Center (CXC) in the application packages CIAO and Sherpa. Optical data were obtained from observations made with the Gran Telescopio Canarias (GTC), installed at the Spanish Observatorio del Roque de los Muchachos of the Instituto de Astrofísica de Canarias, on the island of La Palma. Archival optical data were obtained as part of the INT Photometric Hα Survey of the Northern Galactic Plane (IPHAS; www.iphas.org) carried out at the Isaac Newton Telescope (INT). The INT is operated on the island of La Palma by the Isaac Newton Group in the Spanish Observatorio del Roque de los Muchachos of the Instituto de Astrofisica de Canarias. All IPHAS data are processed by the Cambridge Astronomical Survey Unit, at the Institute of Astronomy in Cambridge. The band-merged DR2 catalog was assembled at the Centre for Astrophysics Research, University of Hertfordshire, supported by STFC grant ST/J001333/1. Funding for the Sloan Digital Sky Survey V has been provided by the Alfred P. Sloan Foundation, the Heising-Simons Foundation, the National Science Foundation, and the Participating Institutions. SDSS acknowledges support and resources from the Center for High-Performance Computing at the University of Utah. UKIDSS data were obtained as part of the UKIRT Infrared Deep Sky Survey. Data are also obtained from the Two Micron All Sky Survey, which is a joint project of the University of Massachusetts and the Infrared Processing and Analysis Center/California Institute of Technology, funded by the National Aeronautics and Space Administration and the National Science Foundation. This work is also based in part on observations made with the Spitzer Space Telescope, which was operated by the Jet Propulsion Laboratory, California Institute of Technology under a contract with NASA. M.G.G. acknowledges the grant PRIN-INAF 2012 (P.I. E. Flaccomio). N.J.W. acknowledges a Royal Astronomical Society Research Fellowship. They also have been supported by the Chandra grant GO0-11040X during the course of this work. J.J.D. and V.K. were supported by NASA contract NAS8-03060 to the Chandra X-ray Center and thank the Director, B. Wilkes, and the CXC science team for advice and support. M.G.G. also

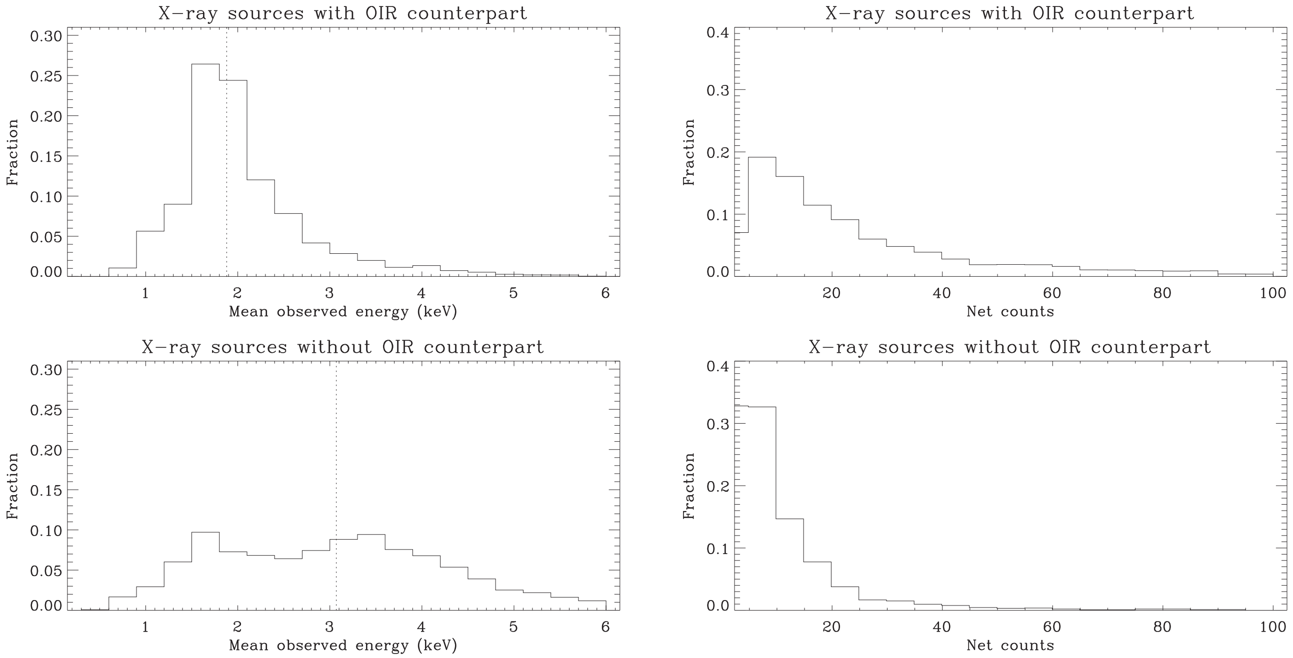

Figure 11. Distributions of the median photon energy (left panels) and net counts (right panels) of the X-ray sources with (top panels) and without (bottom panels) OIR counterparts. The vertical dotted lines in the left panels mark the median values of the distributions.

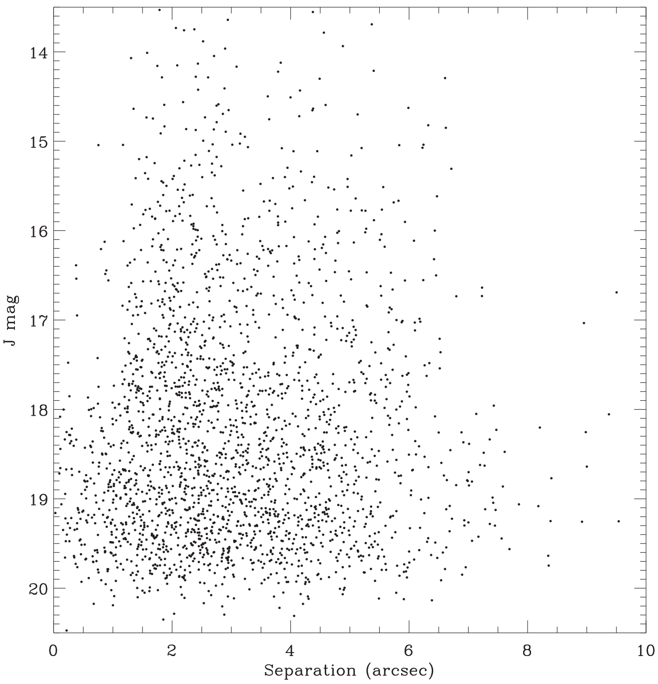

Figure 12. Distribution of the J magnitude of the closest OIR sources to the unmatched X-ray sources vs. their angular separation.

acknowledges J. E. Drew for her important advice and help in the reduction and analysis of the OSIRIS and IPHAS data.

Appendix
Merged Multiband Catalog

Two tables available in electronic format and described in this appendix summarize the photometric properties in optical, infrared, and X-ray bands of all the X-ray sources with optical/infrared counterparts. Source info can be crossmatched using the *ID* values (a progressive number) and *CXO_ID* defined in Wright et al. (2023a). Because of the multiple matches between X-ray and OIR counterparts, *ID* is the truly unique source identifier.

1. The main table (Table A1) includes stellar positions, physical properties, and how the source is classified according to Kashyap et al. (2023). Stellar parameters such as mass, age, and extinction are provided only for members. Individual masses and ages are calculated by interpolating source position in the r versus $r-i$ or J versus $J-K$ dereddened diagrams with a grid of isochrones from the MIST models (Choi et al. 2016) with ages ranging from 0.5 to 10 Myr. Individual extinctions are calculated from the displacement along the extinction vector from the $A_V = 0$, 3.5 Myr isochrone in the $r-i$ versus $i-z$ diagram or adopting the Near-Infrared Color Excess Revisited (NICER) algorithm (Lombardi & Alves 2001), as explained in detail in Kashyap et al. (2023). The table also contains the best photometry available in optical (*guriz*) and infrared *JHK* bands. When available, the best optical photometry is taken from the OSIRIS catalog if it meets the criteria for good photometry defined in Guarcello et al. (2012). If these requirements are not met, then the best optical photometry is taken from the SDSS/DR9 catalog if available or from the IPHAS/DR2 catalog. The latter is transformed into the SDSS photometric system adopting the transformations calculated by Guarcello et al. (2012). The primary choice for the best photometry in the *JHK* bands is the UKIDSS catalog. When it is not available or of bad quality, it is taken from the 2MASS/PSC catalog.
2. The secondary table contains individual counterparts in the optical/infrared catalogs merged in the given source in our multiband catalog (Table A2), together with the results of the matching process.

Since it is expected that the vast majority of the stars associated with Cyg OB2 detected in our X-ray survey should

Table A1
Columns in the Main Table

Column	Description
ID	Progressive number
CXO_ID	X-ray source ID in the Wright et al. (2023a) catalog
R.A.	Source R.A. in J2000
Decl.	Source decl. in J2000
Classification	Source classification according to the Kashyap et al. (2023) Bayesian method
AV	Individual extinction (in magnitudes) in the *V* band for members calculated adopting the Fukugita et al. (1996) extinction law in SDSS bands
AV_err	Uncertainty on A_V (in magnitude)
AV_TAG	Tag explaining how A_V is calculated; possible values are (i) *rri* (e.g., dereddening source position in the $r - i$ versus $i - z$ diagram on adopted $A_V = 0$ isochrone); (ii) NICER (Lombardi & Alves 2001, applied on 2MASS photometry); (iii) NICER_UK (Lombardi & Alves 2001, applied on UKIDSS photometry); (iiii) spectroscopy (for sources with known spectral type)
MASS	Source mass in units of $M_\odot$
AGE	Source age (log of Myr)
DISK	Tag indicating whether the source has a disk (Guarcello et al. 2013) and providing information on disk morphology; see Guarcello et al. (2013) for details on possible tag values
SPT	Source spectral type based on spectroscopic studies
SPT_TAG	Reference for spectral classification; possible values are (i) *S58* (Schulte 1958), (ii) *MT91* (Massey & Thompson 1991), (iii) *C02* (Comerón et al. 2002)
AV_FM07	As AV tag but adopting the Fitzpatrick & Massa (2007) extinction law in SDSS bands
MASS_FM07	As MASS tag but adopting the Fitzpatrick & Massa (2007) extinction law in SDSS bands
AGE_FM07	As AGE tag but adopting when necessary the Fitzpatrick & Massa (2007) extinction law in SDSS bands
MAGU	Magnitude in SDSS *u* band
ERRMAGU	Error associated with MAGU
MAGG	Magnitude in SDSS *g* band
ERRMAGG	Error associated with MAGG
MAGR	Magnitude in *r* band from the best optical catalog
ERRMAGR	Error associated with MAGR
MAGI	Magnitude in *i* band from the best optical catalog
ERRMAGI	Error associated with MAGI
MAGZ	Magnitude in *z* band from the best optical catalog
ERRMAGZ	Error associated with MAGZ
MAGJ	Magnitude in *J* band from the best NIR catalog
ERRMAGJ	Error associated with MAGJ
MAGH	Magnitude in *H* band from the best NIR catalog
ERRMAGH	Error associated with MAGH
MAGK	Magnitude in *K* band from the best NIR catalog
ERRMAGK	Error associated with MAGK
MAG1	Magnitude in [3.6] IRAC band
ERRMAG1	Error associated with MAG1
MAG2	Magnitude in [4.5] IRAC band
ERRMAG2	Error associated with MAG2
MAG3	Magnitude in [5.8] IRAC band
ERRMAG3	Error associated with MAG3
MAG4	Magnitude in [8.0] IRAC band
ERRMAG4	Error associated with MAG4
MAGMIPS	Magnitude in [24.0] MIPS band
ERRMAGMIPS	Error associated with MAGMIPS
FLUX_XRAY_FULL	Energy flux in erg $\mathrm{cm}^{-2}\,\mathrm{s}^{-1}$ in the X-ray full energy band (Wright et al. 2023a; Flaccomio et al. 2023).
PROB_NO_SOURCE	Probability associated with the null hypothesis for the X-ray source of being a background fluctuation, calculated using ACIS extract software by Wright et al. (2023a)

have an OIR counterpart, at least in the UKIDSS catalog, we provide two tables summarizing the optical/infrared properties of the OIR sources closest to each unmatched X-ray source that is classified as a “member” by Kashyap et al. (2023):

1. The table *closest_oir_photometric_table* shares the same format of the *main_table*. It summarizes the photometry of the closest OIR source to each unmatched X-ray source classified as member and identified by means of its CXO_ID (Wright et al. 2023a). The table also shows the position (R.A. and decl.) of the closest OIR source and the separation (in arcseconds) between the two sources.

Table A2
Columns in the Secondary Table

Column	Description
ID	Progressive number
CXO_ID	X-ray source ID in the Wright et al. (2023a) catalog
MAGR_OS	Magnitude in OSIRIS *r* band
ERRMAGR_OS	Error associated with MAGR_OS
MAGI_OS	Magnitude in OSIRIS *i* band
ERRMAGI_OS	Error associated with MAGI_OS
MAGZ_OS	Magnitude in OSIRIS *z* band
ERRMAGZ_OS	Error associated with MAGZ_OS
CHI	Combined χ^2 parameter describing the goodness of the PSF fit on OSIRIS images (Guarcello et al. 2012)
SHARP	*Sharp* parameter from the OSIRIS images (Guarcello et al. 2012)
MAGR_IP	Magnitude in IPHAS *R* band, from DR2 if available, otherwise DR1
ERRMAGR_IP	Error associated with MAGR_IP
MAGI_IP	Magnitude in IPHAS *I* band, from DR2 if available, otherwise DR1
ERRMAGI_IP	Error associated with MAGI_IP
MAGHA	Magnitude in IPHAS Hα band, from DR2 if available, otherwise DR1
ERRMAGHA	Error associated with MAGHA
MAGU	Magnitude in SDSS/DR9 *u* band
ERRMAGU	Error associated with MAGU
MAGG	Magnitude in SDSS/DR9 *g* band
ERRMAGG	Error associated with MAGG
MAGR_SD	Magnitude in SDSS/DR9 *r* band
ERRMAGR_SD	Error associated with MAGR_SD
MAGI_SD	Magnitude in SDSS/DR9 *i* band
ERRMAGI_SD	Error associated with MAGI_SD
MAGZ_SD	Magnitude in SDSS/DR9 *z* band
ERRMAGZ_SD	Error associated with MAGZ_SD
SDSS_CLASS	Classification based on SDSS photometry
MAGJ_2M	Magnitude in 2MASS *J* band
ERRMAGJ_2M	Error associated with MAGJ_2M
MAGH_2M	Magnitude in 2MASS *H* band
ERRMAGH_2M	Error associated with MAGH_2M
MAGK_2M	Magnitude in 2MASS *K* band
ERRMAGK_2M	Error associated with MAGK_2M
PHQUAL	Quality flag from 2MASS/PSC catalog
RDFLAG	Quality flag from 2MASS/PSC catalog
BLFLAG	Quality flag from 2MASS/PSC catalog
CCFLAG	Quality flag from 2MASS/PSC catalog
MAGJ_UK	Magnitude in UKIDSS *J* band
ERRMAGJ_UK	Error associated with MAGJ_UK
MAGH_UK	Magnitude in UKIDSS *H* band
ERRMAGH_UK	Error associated with MAGH_UK
MAGK_UK	Magnitude in UKIDSS *K* band
ERRMAGK_UK	Error associated with MAGK_UK
COLJK_UK	UKIDSS $J - K$ color
ERRCOLJK_UK	Error associated with COLJK_UK
COLHK_UK	UKIDSS $H - K$ color
ERRCOLHK_UK	Error associated with COLHK_UK
MULTI_OPT	Number of multiple coincidences between the OSIRIS, IPHAS, or SDSS counterparts of this source; for single matches it is equal to 0
MULTI_UK_2M	Number of multiple coincidences between the UKIDSS and 2MASS counterparts of this source; for single matches it is equal to 0
MULTI_NIR_OPT	Number of multiple coincidences between the optical and infrared counterparts of this source; for single matches it is equal to 0
MULTI_OIR_IRAC	Number of multiple coincidences between the optical+JHK and IRAC counterparts of this source; for single matches it is equal to 0
MULTI_OIR_X	Number of multiple coincidences involving the OIR and X-ray counterparts of this source; for single matches it is equal to 0
DIST_OIR_X	Distance between the OIR and the X-ray counterparts in arcseconds
REL_OIR_X	Reliability of the OIR versus X-ray coincidence as defined with the modified Smith et al. (2011) method
TAG_PM	Equal to 1 if the OIR and X-ray counterparts have been matched by the PM matching method
TAG_SM	Equal to 1 if the OIR and X-ray counterparts have been matched by the modified Smith et al. (2011) method
TAG_NB_I	Equal to 1 if the OIR and X-ray counterparts have been matched by the Bayesian matching procedure defined by Naylor et al. (2013) applied using the MAGI values
TAG_NB_K	Equal to 1 if the OIR and X-ray counterparts have been matched by the Bayesian matching procedure defined by Naylor et al. (2013) applied using the MAGK values

Table A2
(Continued)

Column	Description
TAG_NB_IRAC	Equal to 1 if the OIR and X-ray counterparts have been matched by the Bayesian matching procedure defined by Naylor et al. (2013) applied using the MAG1 values
RELIABLE_MATCH	Equal to 1 if the OIR-X-ray match is "reliable"
SUGGESTED_COUNTERPART	Equal to 1 if the source is a multiple OIR versus X-ray identification (MULTI_OIR_X>1) and this coincidence has been set as the most reliable by visual inspection of positions and OIR diagrams; single matches always have SUGGESTED_COUNTERPART=1

2. The table *closest_oir_secondary_table* shows individual counterparts in the optical/infrared catalogs.

ORCID iDs

M. G. Guarcello https://orcid.org/0000-0002-3010-2310
J. J. Drake https://orcid.org/0000-0002-0210-2276
T. Naylor https://orcid.org/0000-0002-0506-8501
E. Flaccomio https://orcid.org/0000-0002-3638-5788
V. L. Kashyap https://orcid.org/0000-0002-3869-7996

References

Aihara, H., Allende Prieto, C., An, D., & Anderson, S. F. E. A. 2011, ApJS, 193, 29
Albacete Colombo, J. F., Flaccomio, E., Micela, G., Sciortino, S., & Damiani, F. 2007, A&A, 464, 211
Barentsen, G., Farnhill, H. J., Drew, J. E., et al. 2014, MNRAS, 444, 3230
Beerer, I. M., Koenig, X. P., Hora, J. L., et al. 2010, ApJ, 720, 679
Bica, E., Bonatto, C., & Dutra, C. M. 2003, A&A, 405, 991
Broos, P. S., Townsley, L. K., Feigelson, E. D., et al. 2010, ApJ, 714, 1582
Casali, M., Adamson, A., Alves de Oliveira, C., et al. 2007, A&A, 467, 777
Cepa, J., Aguiar, M., & Escalera, E. A 2000, Proc. SPIE, 4008, 623
Choi, J., Dotter, A., Conroy, C., et al. 2016, ApJ, 823, 102
Comerón, F., Pasquali, A., Rodighiero, G., et al. 2002, A&A, 389, 874
Cutri, R. M., Skrutskie, M. F., van Dyk, S., et al. 2003, 2MASS All Sky Catalog of Point Sources
Damiani, F., Maggio, A., Micela, G., & Sciortino, S. 1997, ApJ, 483, 350
Drew, J. E., Greimel, R., Irwin, M. J., et al. 2005, MNRAS, 362, 753
Drew, J. E., Greimel, R., Irwin, M. J., & Sale, S. E. 2008, MNRAS, 386, 1761
Dye, S., Warren, S. J., Hambly, N. C., et al. 2006, MNRAS, 372, 1227
Fitzpatrick, E. L., & Massa, D. 2007, ApJ, 663, 320
Flaccomio, E., Albacete-Colombo, J. F, Drake, J. J., et al. 2023, ApJS, 269, 12
Flaherty, K. M., Pipher, J. L., Megeath, S. T., et al. 2007, ApJ, 663, 1069
Fukugita, M., Ichikawa, T., Gunn, J. E., et al. 1996, AJ, 111, 1748
Garmire, G. P., Bautz, M. W., Ford, P. G., Nousek, J. A., & Ricker, G. R., Jr. 2003, Proc. SPIE, 4851, 28
Gilmour, R., Gray, M. E., Almaini, O., et al. 2007, MNRAS, 380, 1467
Guarcello, M. G., Damiani, F., Micela, G., et al. 2010, A&A, 521, A18
Guarcello, M. G., Drake, J. J., Wright, N. J., et al. 2013, ApJ, 773, 135
Guarcello, M. G., Wright, N. J., Drake, J. J., et al. 2012, ApJS, 202, 19
Hanson, M. M. 2003, ApJ, 597, 957
Hewett, P. C., Warren, S. J., Leggett, S. K., & Hodgkin, S. T. 2006, MNRAS, 367, 454
Kashyap, V. L., Guarcello, M. G., Wright, N. J., et al. 2023, ApJS, 269, 10
Kim, M., Kim, D.-W., Wilkes, B. J., et al. 2007, ApJS, 169, 401
King, R. R., Naylor, T., Broos, P. S., Getman, K. V., & Feigelson, E. D. 2013, ApJS, 209, 28
Knödlseder, J. 2000, A&A, 360, 539
Lombardi, M., & Alves, J. 2001, A&A, 377, 1023
Lucas, P. W., Hoare, M. G., Longmore, A., et al. 2008, MNRAS, 391, 136
Massey, P., & Thompson, A. B. 1991, AJ, 101, 1408
Naylor, T., Broos, P. S., & Feigelson, E. D. 2013, ApJS, 209, 30
Negueruela, I., Marco, A., Herrero, A., & Clark, J. S. 2008, A&A, 487, 575
O'Donnell, J. E. 1994, ApJ, 422, 158
Reddish, V. C., Lawrence, L. C., & Pratt, N. M. 1967, PROE, 5, 112
Richter, G. A. 1975, AN, 296, 65
Rieke, G. H., & Lebofsky, M. J. 1985, ApJ, 288, 618
Rumbaugh, N., Kocevski, D. D., Gal, R. R., et al. 2012, ApJ, 746, 155
Rygl, K. L. J., Brunthaler, A., Sanna, A., et al. 2012, A&A, 539, A79
Sale, S. E., Drew, J. E., Barentsen, G., et al. 2014, MNRAS, 443, 2907
Sale, S. E., Drew, J. E., Unruh, Y. C., et al. 2009, MNRAS, 392, 497
Schulte, D. H. 1958, ApJ, 128, 41
Siess, L., Dufour, E., & Forestini, M. 2000, A&A, 358, 593
Smith, D. J. B., Dunne, L., Maddox, S. J., et al. 2011, MNRAS, 416, 857
Sutherland, W., & Saunders, W. 1992, MNRAS, 259, 413
Taylor, E. L., Mann, R. G., Efstathiou, A. N., et al. 2005, MNRAS, 361, 1352
Vink, J. S., Drew, J. E., Steeghs, D., et al. 2008, MNRAS, 387, 308
Walborn, N. R. 1973, ApJL, 180, L35
Wright, N. J., & Drake, J. J. 2009, ApJS, 184, 84
Wright, N. J., Drake, J. J., Drew, J. E., et al. 2012, ApJL, 746, L21
Wright, N. J., Drake, J. J., Drew, J. E., & Vink, J. S. 2010, ApJ, 713, 871
Wright, N. J., Drake, J. J., Guarcello, M. G., et al. 2023a, ApJS, 269, 7
Wright, N. J., Drake, J. J., Guarcello, M. G., Kashyap, V. L., & Zezas, A. 2023b, ApJS, 269, 8
Wright, N. J., Drew, J. E., & Mohr-Smith, M. 2015b, MNRAS, 449, 741
Wright, N. J., Greimel, R., Barlow, M. J., et al. 2008, MNRAS, 390, 929
Wright, N. J., Parker, R. J., Goodwin, S. P., & Drake, J. J. 2014b, MNRAS, 438, 639